Structural, morphological and photoluminescent properties of Nd-coated silicon nanostructures

Amine Mefoued[1,2]*, Bedra Mahmoudi[1], Nasser Benrekaa[2], Faiza Tiour[1], Hamid Menari[1], Abdelyamine Naitbouda[3], Amar Manseri[1], Afaf Brik[1], Salah Mezghiche[1], Moustafa Debbab[4]

[1]Centre de Recherche en Technologie des Semi-conducteurs pour l'Énergétique (CRTSE), 02 Bd Frantz Fanon BP140, Alger–7 merveilles, 16027 Algiers, Algeria

[2]Faculté de Physique, Université des Sciences et de la Technologie Houari Boumediene (USTHB), BP 32 Bab-Ezzouar, 16111 Algiers, Algeria

[3]Centre de Développement des Technologies Avancées (CDTA), Cité 20 août 1956, 16081 Algiers, Algeria

[4]Université Abou Bekr Belkaid BP 230, 13000 Chetouane, Tlemcen, Algeria

Article info	Abstract
	The structural, morphological and photoluminescent properties of thermally evaporated neodymium oxide (Nd_2O_3) thin films deposited onto nanostructured silicon (Si-ns) are reported. Si-ns embedded in silicon nitride (SiN) thin films are prepared by plasma-enhanced chemical vapour deposition (PECVD). SiN and Nd_2O_3 thin films uniformity and Si-ns formation are confirmed by atomic force microscopy (AFM) and scanning electron microscopy (SEM). The presence of neodymium (Nd), silicon (Si), oxygen (O), and phosphorus (P) is investigated by energy-dispersive spectroscopy (EDS) and secondary ion mass spectrometry (SIMS). Post-annealing SIMS profile indicates an improvement of the homogeneity of activated P distribution in Si bulk. The X-ray diffraction (XRD) combined with Raman spectroscopy and Fourier-transform infrared spectroscopy (FTIR) have been employed to determine amorphous silicon (a-Si), crystalline silicon (c-Si), Nd_2O_3 and SiN phases present in the Nd_2O_3-SiN bilayers with their corresponding chemical bonds. After annealing, a Raman shift toward lower wavenumbers is recorded for the Si peak. XPS data reveal the formation of Nd_2O_3 thin films with Nd-O bonding incorporating trivalent Nd ions ($Nd3+$). Strong room-temperature photoluminescence is recorded in the visible light range from the Si-ns. Nd-related photoluminescent emission in the near infrared (NIR) range is observed at wavelengths of 1025–1031 nm and 1083 nm, and hence is expected to improve light harvesting of Si-based photovoltaic devices.

1. Introduction

Over the past years, a growing interest has been focused on silicon nanostructures (Si-ns) or nanoparticles with applications in microelectronics [1], photonics [2], biology [3], biomedicine [4], and other emerging fields [5–7]. Si-ns emit light in the visible due to the recombination of confined excitons within the nanostructure material [8, 9]. For the so-called third generation photovoltaic (PV) solar cells, absorption, and emission of light by Si-ns thin films could be enhanced along with the device efficiency by optimizing silicon nanocrystal (Si-nc) design and their size-dependence to the band gap [10–12]. It was also observed that surface modification induces different emission wavelengths and yields a significant improvement in photoluminescence (PL) emission, an important characteristic for photonics and photovoltaics. Furthermore, these thin films possess optical and structural properties related to their nanostructured nature and could host some rare-earth (RE) elements (or lanthanides) like erbium (Er), europium (Eu), or neodymium (Nd) using either ion implantation or thin film deposition with electrochemical

[13], sputtering [14], or thermal evaporation [15] techniques. Nd^{3+} ions can display PL up-conversion phenomenon. Up-conversion is a non-linear anti-Stocks optical process in which an excitation with low energy photons of the near infrared (NIR) range will generate high energy photons (visible range) [16, 17]. The sensitizing effect [18] happening in a system where RE elements and Si-ncs are 'working together' to capture and redistribute photons is the key to achieve efficient optical devices. The absorption of an up-converter like Nd and the sensitizing process of Si-nc toward Nd^{3+} ions, where energy transfer occurs between them, have been discussed in detail [19, 20]. A direct correlation between Si-nc average size and the PL intensity of the Nd-embedded Si-nc matrix was also observed by some authors. As a result of the NIR emission demonstrated by Nd^{3+} ions, Nd-coated Si-ncs prepared by plasma-enhanced chemical vapour deposition (PECVD) technique [21] are well placed to offer interesting up-conversion properties and significantly improve PV solar cells performance.

In the present work, the authors intend to support and extend previous studies about Si-nc-related morphological, structural, and spectroscopic properties and RE elements doping. Samples consisting of Si-ns embedded within SiN$_x$ thin films were prepared. Experimental results indicated the size and degree of crystallinity dependence of the optical band gap inherent to the nanostructured state of Si. A strong visible PL can be observed in SiN$_x$ and the evolution of PL with the NH$_3$/SiH$_4$ gas ratio is correlated with the SiN$_x$ structure evolution. It also resulted in the increase of the refractive index with SiN films having an excess of Si. The existence of an increased absorption on the high energy side is associated with Si-ncs. The optical gap varies from 2.4 eV for the ratio of NH$_3$/SiH$_4$ = 6 to 1.3 eV for silicon rich SiN$_x$ at NH$_3$/SiH$_4$ = 0.5 [22, 23]. Further investigations were undergone to assess the effect of Eu incorporation into SiN$_x$ matrix (comprising the nanostructures). For that purpose, an innovative and cost-effective electrochemical technique is used to insert successfully Eu into the silicon-rich silicon nitride (SRSN) films at a low temperature and atmospheric pressure conditions [24]. In this sense, investigations will focus on the spectroscopy and opto-structural properties of Nd-coated Si-nc and the suitability of these low-dimensional materials for PV applications.

2. Experimental

2.1. Synthesis and samples preparations

Silicon nitride (SiN$_x$) thin films have been deposited by low frequency plasma-enhanced chemical vapour deposition (LF-PECVD) at 430 kHz on (100) oriented, p-type Czochralski single crystal Si wafers using silane-ammonia (SiH$_4$-NH$_3$) reactants gases. The host substrates are 380 μm thick and have resistivities of 1–3 Ω·cm. Prior to SiN deposition, the wafers were subjected to a thermal diffusion process (875°C/1 h) in a quartz furnace using liquid phosphorus oxychloride (POCl$_3$) as the dopant source. A pn junction with a depth of 0.5 μm was obtained. PECVD gas flow ratios (R = NH$_3$/SiH$_4$) were fixed at 2, 2.5, 3, 4, and 5. For simplicity of notation, we will refer to samples

prepared at R = 2, 2.5, 3, 4, and 5 as R2, R2.5, R3, R4, and R5, respectively. The pressure, temperature, deposition time and plasma power conditions were kept constant at 1700 mT, 380 °C, 3 min., and 4.6 kW for all processes. Evaporation of neodymium oxide (Nd$_2$O$_3$) powder on top of the SiN$_x$ layer was performed using a lab-designed evaporator. A heat treatment in quartz tube furnace at 900 °C for 15 min. under N$_2$ flow followed the Nd$_2$O$_3$ thin film formation.

Silicon wafers were purchased from Siltronix. All chemicals were used as received without further purification. All cleaning and etching reagents used in this study such as acetone (98%), ethanol (> 99.8%), sulphuric acid (98%), oxygen peroxide (30%), and hydrogen fluoride (50%) were obtained from Sigma-Aldrich. Nd (99%) powder was purchased from Sigma-Aldrich. Silane (SiH$_4$, ultrahigh purity) and ammonia gas (NH$_3$, ultrahigh purity) were purchased from Air Products.

The flowchart of all processing steps and the schematic view of the samples cross-sectional structure are shown in Fig. 1.
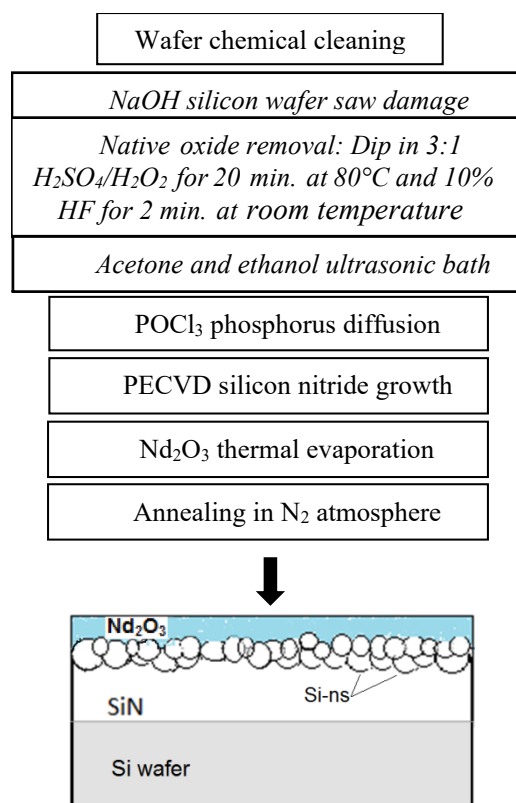

Fig. 1. Flowchart of the sample preparation steps and cross-section structure of the samples.

2.2. Instruments

Diffusion process and PECVD thin films deposition were carried out in two separate quartz tubes from SEMCO Engineering. Post Nd evaporation calcination was done in a Tempress Omega Junior furnace. Four-point probe electrical resistivity was measured using a Chang Min Tech Co. instrument. Surface reflection was obtained using a Varian Cary 500 UV-Visible spectrophotometer equipped with a diffuse-reflectance attachment. XRD patterns were

recorded on an XRD Ultima IV (Rigaku) diffractometer using monochromatic Cu*Kα* radiation ($\lambda = 1.54059$ Å). The voltage generator and tube current were 40 kV and 40 mA, respectively. The slew rate was 5°/min. with a step of 0.1°. The morphology of the surface was characterised using a JEOL JSM-7610FPlus field emission scanning electron microscope (FESEM). Thickness was examined on cross-sections of the layers from a fracture of the samples. The JSM-7610FPlus integrates an energy dispersive X-ray spectroscope (EDS) to determine the layer chemical composition, as well as possible contaminants. The samples were analysed without any prior sputtering process. Additional morphological observations of the surface were done using an MFP-3D atomic force microscope (AFM) from Oxford Instruments. Raman spectroscopic measurements were performed using a LabRAM HR Evolution system spectroscope (Horiba Jobin-Yvon). The excitation of the Raman spectra was provided by a solid-state laser emitting at 325 nm with 32 mW power. The Raman spectra covering the range of frequency shift from 50 cm^{-1} to 2500 cm^{-1} were obtained at room temperature. Secondary ion mass spectrometry (SIMS; Cameca IMS 4FE7) was used to probe the surface. An incident 80 nA and 15 keV Cs+ ion beam was scanned across a 150 µm diameter probe area to gather information about the sample and extract chemical elements depth-profiles. IR spectra were collected using a NEXUS 670 standard Fourier-transform infrared (FTIR) spectrometer (from Thermo Nicolet). X-ray photoelectron spectroscopy (XPS) measurements were done on a Thermo Fisher ESCALAB 250*Xi* using monochromatic Al-*Kα* source with a spot diameter of 650 µm and an energy step of 0.1 eV. Binding energy (BE) data were calibrated with respect of the characteristic carbon (C *1 s*) peak situated at 284.8 eV using Avantage software provided by the manufacturer. The PL spectra were collected using a HORIBA spectrometer iHR-550 equipped with an indium-gallium-arsenide (InGaAs) detector (DSS-IGA020L) working in the NIR range of 800–1550 nm and another CCD detector operating in the range of 200–1000 nm. The room temperature PL was performed using either He-Cd laser or Xe lamp as excitation sources.

3. Results and discussion

3.1. Reflectance and optical band gap calculations

UV-visible reflectance was measured for samples prepared at various process conditions (plasma gas ratio *R*, Nd$_2$O$_3$ deposition, annealing) as a function of the wavelength. We observed that for all samples the reflectance in the visible range decreases after annealing (900 °C 15 min.) as depicted in Fig. 2 for sample R4.

Reflectance of SiN$_x$-coated samples before evaporating Nd$_2$O$_3$ thin film is plotted in Fig. 3(a). The highest average reflectance (17%) is measured for thin films grown at $R = 2.5$. As we start to increase the ammonia-silane (NH$_3$/SiH$_4$) ratio, we noticed a reduction in the reflectance.

Figures 3(b) and 3(c) represent the reflectance of the double layered (Nd$_2$O$_3$/SiN$_x$) samples before and after annealing at 900 °C for 15 min. A decrease in the reflectance is seen after adding the Nd$_2$O$_3$ thin films in the range of 700–1000 nm and again after undertaking thermal
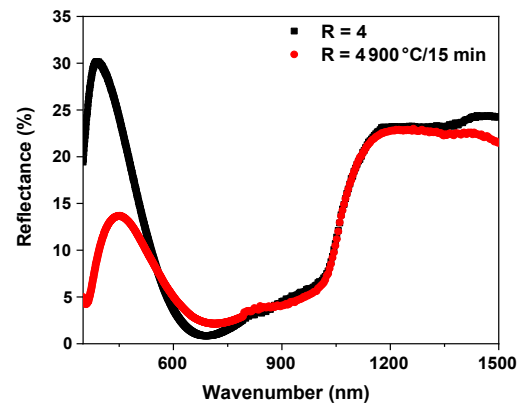

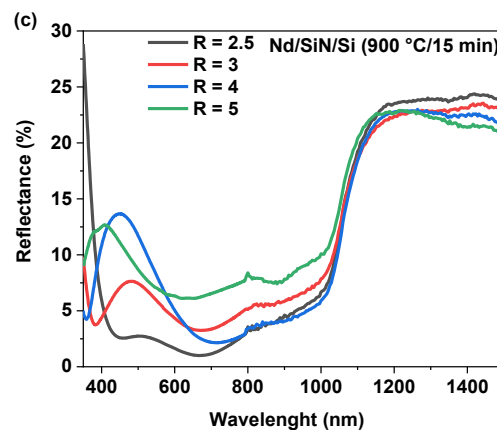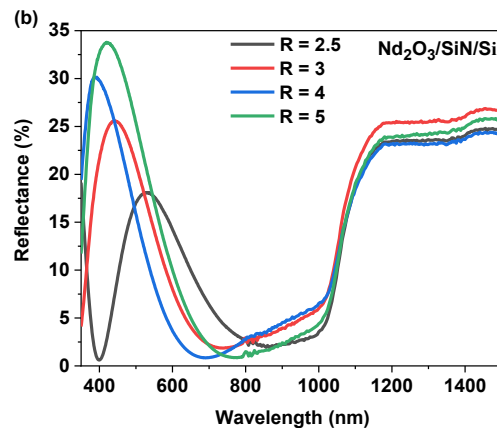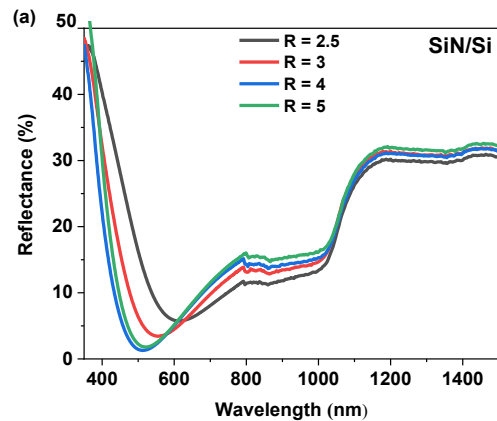**Fig. 2.** Effect of thermal annealing on the shape of a sample prepared in ratio 4.

Fig. 3. Reflectance spectra for samples prepared at different steps and PECVD NH$_3$/SiH$_4$ gas ratios after adding the Nd$_2$O$_3$ layer on-top of SiN$_x$ and subsequent calcination process.

annealing process independently of the NH_3/SiH_4 gas ratio in the blue region of 400–600 nm. The lowest calculated average reflectance in the spectral range of 350–800 nm is 3.61% around a wavelength of 675 nm for the annealed Nd_2O_3-coated sample prepared at $R = 2.5$. Similar conclusions pertaining to bilayers reflectance were confirmed by the authors elsewhere [25].

Band gap energies (Eg) were calculated from diffuse reflectance spectra for annealed Nd_2O_3-coated samples using the Kubelka-Munk function (Fig. 4) and their resulting Tauc plots [26]. In Fig. 5, we can see that optical gap of SiN_x-coated samples increases simultaneously when increasing gas ratio during PECVD Si-ns growth and reaches a maximum value of ~2 eV. The narrowing of optical gap is correlated to higher proportion of Si in the films which is true for thin films prepared at a low NH_3/SiH_4 ratio [27] in good agreement with findings reported in the literature that bandgap energy increases with decreasing nanostructures size [28].
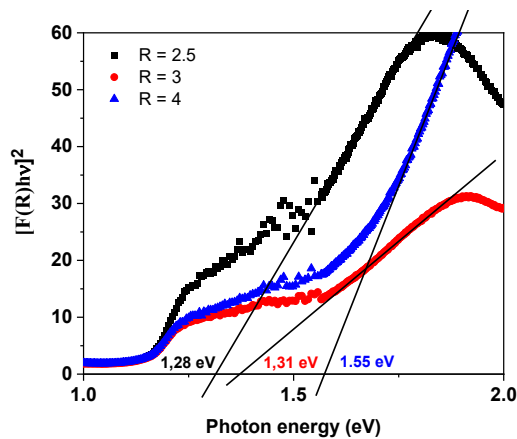

Fig. 4. Bandgap energies calculated by the Kubelka-Munk method for $Nd_2O_3/SiN_x/Si$ samples annealed at 900 °C for 15 min.
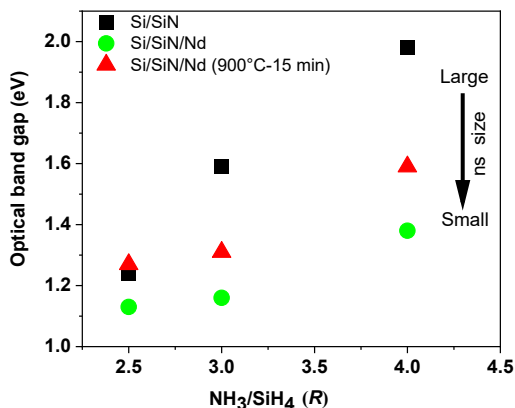

Fig. 5. Evolution of the optical gap *vs.* the NH_3/SiH_4 gas flow ratio for Nd-doped Si-ns.

It should be noticed that the evaporation of the Nd_2O_3 layer has an overall impact on the absorption and optical properties of the wafer surface by lowering Eg values. Obtained results show that the sample prepared at $R = 4$ offers good anti-reflective properties by showing reflectance minima in the visible and near-IR (Vis-NIR) regions. Overall, thin films kept good anti-reflection properties after adding the Nd_2O_3 coating.

3.2. AFM and SEM-EDS

3.2.1. AFM

2D and 3D representative surface plots from AFM analyses are shown in Fig. 6 for SiN-coated Si-nc films obtained at PECVD precursor gas ratio $R = 4$. The topography images show similar morphologies with homogenous surfaces and uniformly distributed particles. Root mean square (RMS) surface roughness was calculated for areas with lateral dimensions of 5×5 μm^2 and 80×80 μm^2. RMS values vary between 2–10 nm for the smaller scanning area and increase to a range of 260–460 nm when considering the larger spot. On the larger scale, all the films surfaces were found to be identically smooth, free of cracks and fracture lines. Morphological differences nano-roughness amplitudes are found to be 1.96 and 2.95 nm for gas flow ratios of 3 and 4, respectively (images not shown here). These results are consistent with previously reported AFM investigations and roughness calculations [29] and could indicate SiN_x layers that are rich in Si due to the increase of NH_3/SiH_4 ratio in the plasma chamber. The excess in Si is important when considering optical applications due to optical loss that light scattering process may cause. Generally, high porosity and nanocrystalline Si formation has significantly high surface roughness on the c-Si wafers [30, 31].
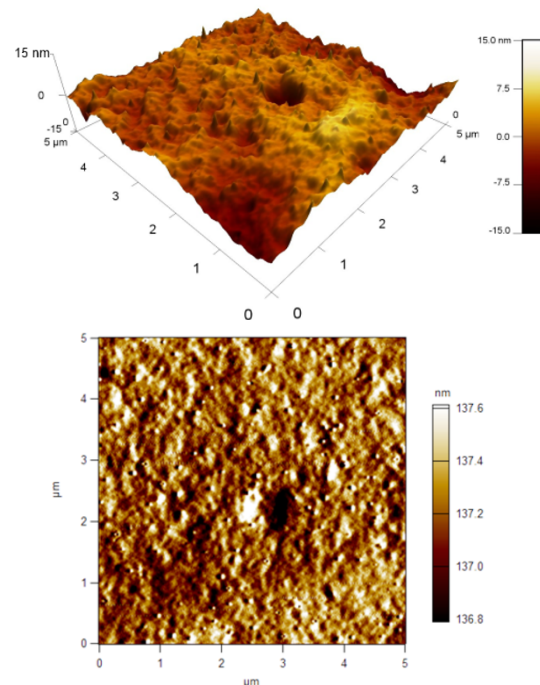

Fig. 6. AFM images of samples prepared at NH_3/SiH_4 $R = 4$.

3.2.2. SEM-EDS

The growth pattern and morphology were examined by a high-resolution scanning electron microscope (SEM). Plane SEM views of selected Nd-coated and uncoated Si-nc films (R4) are shown in Figs. 7(a) and 7(b). The deposited round-like shaped Si agglomerates [Fig. 7(a)] appeared smooth and showed a dense and homogeneous nanostructure without indication of columnar growth. From Fig. 7(b), the image illustrates the evaporated Nd_2O_3 coating covering the nano-structured surface beneath it.

The after-annealing image shows clearly that Nd has partially diffused in the nanostructures as revealed by the islands-like pattern of Nd_2O_3 thin film distribution on the Si nanostructured surface. Thin film thickness estimations obtained from SEM fracture cross-section micrograph depicted in Fig. 7(c) are ~70 nm and 50–55 nm for SiN_x and Nd_2O_3, respectively. These results agree with thickness measurements obtained by contact profilometry giving exact values of 52.25 and 53.54 nm for two different samples. Both Nd_2O_3 and SiN_x films could clearly be distinguished from the cross-section view with a neat interface separation between Nd_2O_3 and SiN and between SiN and Si wafer.

In Fig. 7(d), EDS analysis confirmed the presence of Si, O, N, P. The proportion of Nd remains unchanged for all samples prepared with different gas ratios.

3.3. SIMS

Figure 8 shows quantitative P depth profiles extracted by SIMS for a sample prepared at $R = 2.5$. They follow the typical kink-and-tail profile with two distinct phases [32, 33]. After annealing at 900 °C for 15 min., P diffused further, and the profile is seen broader with a less abrupt feature pointing to a higher P diffusivity and a more homogeneous redistribution in the Si bulk. Diffusion resulted in a maximum P concentration of 1.3×10^{22} cm^{-3} which after annealing decreased approximately by one-seventh to 1.75×10^{21} cm^{-3}. Comparable results were obtained for samples with $R = 3$, 4, and 5 (results not shown here). Phosphorus uniformity and depth-distribution will ensure that diffusion step and formation of the junction are well optimised. These parameters are required to achieve efficient Si-based solar cells.

Nd, O, Si, and N qualitative profiles are displayed in Fig. 9 for a sample prepared at $R = 4$ and calcined at 900 °C for 15 min. Qualitatively, O content is 11 orders of magnitude higher with respect to N at depth between 7 and
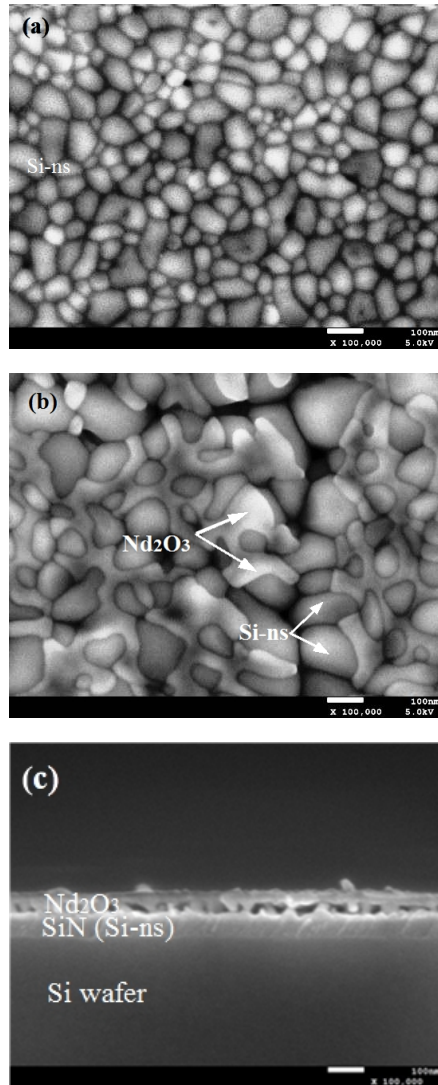

Fig. 7. SEM and EDS images of the sample prepared NH_3/SiH_4 ratio $R = 4$: (a) and (b) plane views of un-coated and Nd_2O_3-coated; (c) cross-section view; (d) EDS elemental mapping.
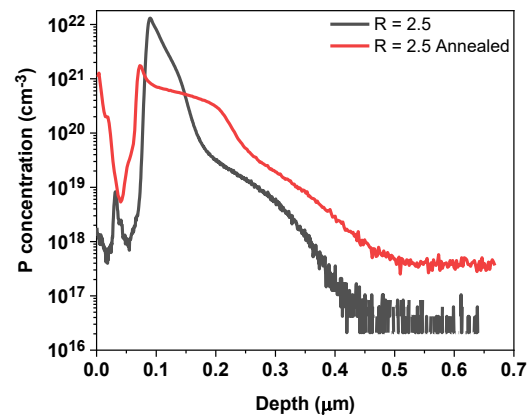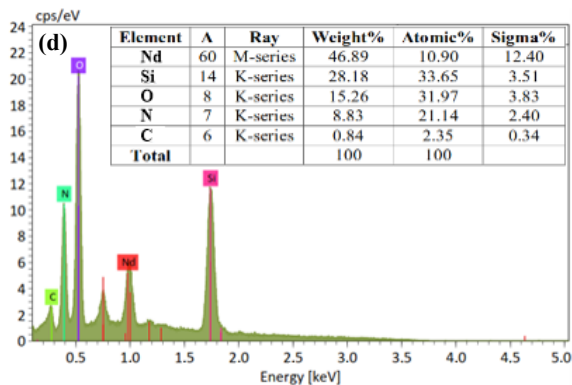

Fig. 8. Effect of annealing on the SIMS depth profiles of P before and after annealing at 900 °C for 15 min.
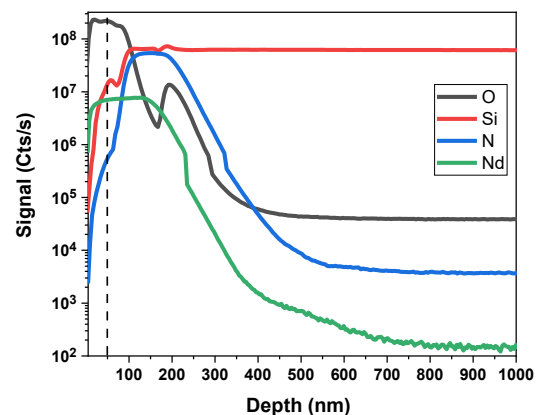

Fig. 9. Qualitative SIMS depth profiles of Si, N, Nd, and O after annealing at 900 °C for the annealed sample R4.

40 nm, which is expected due to the presence of O in the Nd_2O_3 compound. The spectra show N and Si in-depth intensities continuously increasing and stabilising at ~50 nm indicating that we have reached the Nd_2O_3/SiN interface. Interestingly, we noticed the presence of Nd between approximately 50 and 100 nm probably due to the result of annealing-induced Nd species migration in the SiN layer. The Si and N spectra almost overlap between thicknesses of 50 and 90 nm inside the SiN layer. Beyond a depth of 90 nm, we observe that N concentration drops as illustrated by the long tail until stabilising around 250 nm. On the other hand, Si spectrum keeps a flat profile as we sputter through the SiN stack and Si bulk with a small shoulder at ~85 nm as we cross the SiN/Si interface. SIMS analysis of the surface allowed us to determine the presence of the Nd_2O_3 upper layer and evaluate its depth-profile evolution.

3.4. XRD and Raman spectroscopy

Low grazing angle XRD patterns were recorded for the $R = 4$ Nd_2O_3/SiN/Si sample (Fig. 10). The authors were able to identify the main phases composing the structure from the top surface layer down to the Si substrate. Results confirm the above-mentioned elemental composition identified by SIMS and EDX. The SiN peaks were determined and compared to the β-phase SiN datasheet reported in JCPDS library (Datasheet no. 33-1160). Crystallographic orientations (*hkl*) were determined, and average particle size D values were calculated using the Debye-Scherrer equation [34]. Results for SiN are detailed in Table 1 and match perfectly within a margin of ±0.9°.
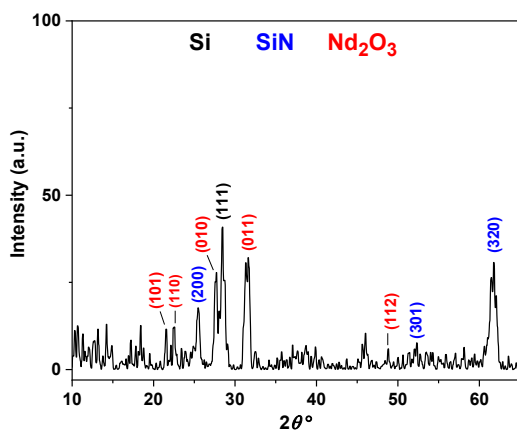

Fig. 10. X-ray diffraction patterns of the annealed Nd_2O_3-coated silicon nanostructures prepared with an NH_3/SiH_4 gas ratio of 4.

Table 1.
Comparison between SiN JCPDS datasheet values and the observed data.

2θ [°] (JCPDS)	2θ [°] (observed)	*h k l*
13.1	13.15	100
25.5	26.4	200
36.0	35.75	111
61.74	61.75	320

A strong and sharp peak belonging to c-Si appears at a position of 69.1°. From the (400)-oriented peak (JCPDS Card no.°77-2110), we estimated D to be ~6.82 nm. Another less intense Si peak appears at 28.5° and could be ascribed to (111) reflection plane. Nd-O XRD patterns exhibit weak diffraction intensities with respect to c-Si and SiN ones. Peaks belonging to hexagonal Nd_2O_3 [35] phase were observed at 21.6°, 22.6°, 27.7°, 31.3°, and 48.9° and were assigned to (101), (110), (010), (011), and (112), respectively. These values match well with data given in JCPDS cards nos.: 28-0671, 41-1089, 74-2139, 43-1023, and 75-2255. Using the above, the Nd_2O_3 average crystallite size was calculated to be 40.7 nm agreeing with comparable findings reported in the literature [36].

First order room temperature Raman spectra of Nd-coated Si-ns were recorded with a laser beam excitation wavelength of 325 nm. All samples exhibit strong and fine peaks between 515 and 518 cm^{-1} corresponding to transverse optical (TO) mode (100) crystalline Si (c-Si) scattering (results not shown here). Figure 11 shows Raman spectra of samples prepared at different gas ratios and annealed at 900 °C for 15 min. This gradual shift to lower frequencies as we increase PECVD gas ratios corresponds to SiN layers being in excess of Si content. We also noticed that the broad signal of R2 Si peak morphs and becomes narrower and more intense with increasing gas ratios. This trend is attributed to the size effect and the refinement of the nanoparticles. The slight frequency downshift of the crystalline peak with its relatively broad bottom part and the presence of Si-ncs of a small size were confirmed by Barbé *et al.* [37]. The average Si crystallite size, extracted from Raman spectra and calculated using the empirical equation proposed by Tsu [38], was found to be 3.36 nm. The quantitative discrepancy between Raman and XRD-calculated grain size values might be explained by the fact that samples used for XRD measurements have undergone a longer thermal process (2 h) at higher temperature (1100 °C) compared to those used for Raman analyses. Another explanation is the use of different mathematical peak fitting functions and procedures to exploit data collected from XRD and Raman analyses [39].
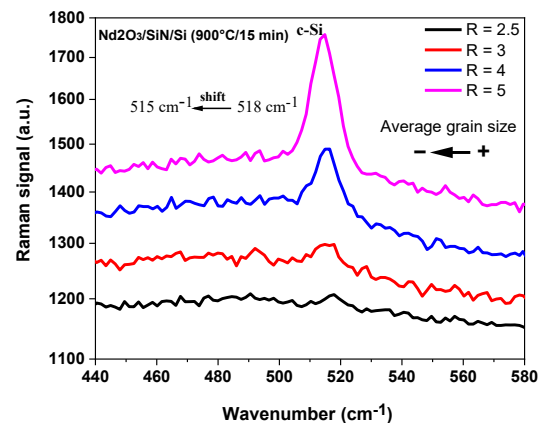

Fig. 11. Evolution of c-Si Raman spectra with different *R*.

Concerning Nd_2O_3 molecule, a relatively small and wide signal is observed at 435 cm^{-1} (Fig. 12) and can be identified as E_g stretching mode [40, 41]. One can also see in Fig. 12 that a peak is observed at 312 cm^{-1} and could be assigned to the Si substrate [42].
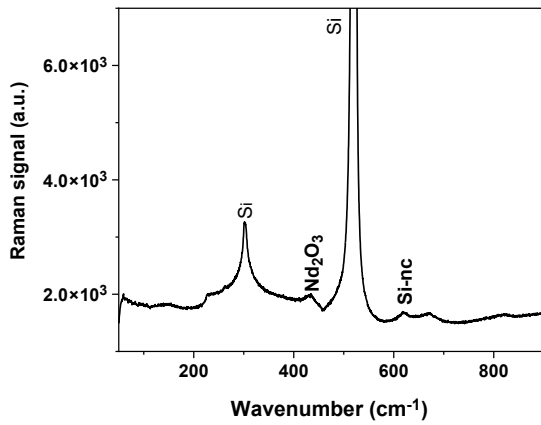
Fig. 12. Raman spectra for the Nd_2O_3-coated sample prepared at gas ratio $R = 4$.

3.5. FTIR

FTIR analysis was performed in the range of 400–4000 cm^{-1} with a 4 cm^{-1} resolution. Each FTIR graph was recorded after 20 scans per sample. Figure 13 shows resonances of compositional bonds found in the Nd_2O_3-SiN bilayers. Characteristic absorption bands of Si-N, Si-O, Nd-O, and Si-H molecular species were detected. For samples R4 and R5, the increase of gas ratio R has an impact on the peak position of the Si-N mode where we notice a size-dependent shift to higher wavenumbers demonstrated by the asymmetric stretching of Si-N bonds appearing at 850 and 856 cm^{-1}, respectively [43, 44]. The Si-O bending mode [45] absorbs around 819 and 823 cm^{-1} for samples R4 and R5, respectively while those at 1103 and 1107 represent the Si-O-Si asymmetric stretching vibrational mode [46]. The appearance of Si-H peaks at 611–615 cm^{-1} (wagging mode) and 2364–2368 cm^{-1} (stretching mode) is synonymous with the occurring of passivation phenomenon, where hydrogen H elements are released during the SiN PECVD process and diffuse deep to passivate electrically active defects at the SiN/c-Si interface and Si bulk, thus reducing recombination of charge-carriers [47]. Finally, peaks at 692 cm^{-1} (for R4) and 684 cm^{-1} (R5) are due to a characteristic vibration of metal-oxygen Nd-O bond [48, 49].
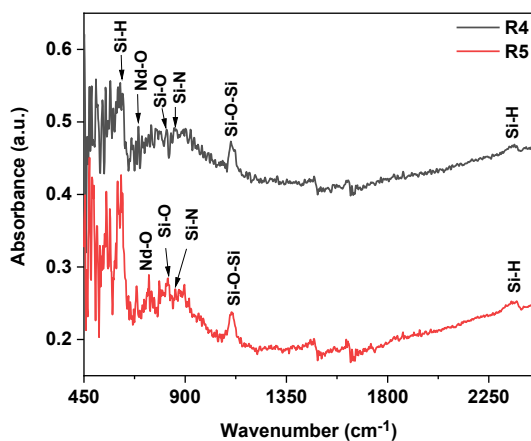

Fig. 13. FTIR spectra of Nd_2O_3-coated Si-ns prepared at NH_3/SiH_4 gas ratios of 4 and 5.

3.6. XPS

To further investigate the surface chemical composition and stoichiometry by high-resolution X-Ray photoelectron spectroscopy (XPS), three sets of samples consisting of as-deposited Si-ns (R2) and Nd_2O_3-coated Si-nc ones (R2.5 and R5) were selected. XPS survey scans (also known as wide scans) performed over a BE range of 0–1400 eV are shown in Figs. 14 and 15. For R2.5 and R5, they showed O $2s$, Nd $4d$, O $1s$, Nd (Auger), Nd $3d_{5/2}$, and Nd $3d_{3/2}$ peaks corresponding to the Nd and O elements of Nd_2O_3. From R2, spectral signals of Si $2p$, Si $2s$, C $1s$, N $1s$, O $1s$, O (Auger) were recorded and assigned to the Si, N and O elements of SiN and probably silicon oxide (SiO_2) molecules. A compilation of BE data and chemical states is presented in Table 2.
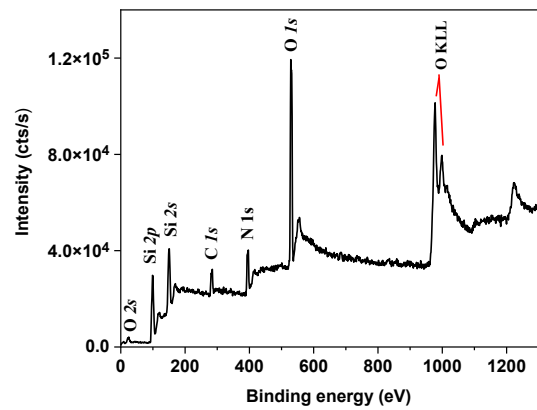

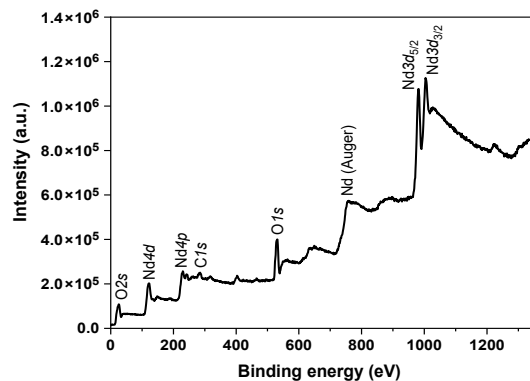**Fig. 14.** Wide scan XPS spectra of as-deposited Si-nc prepared at $R = 2$.

Fig. 15. Wide scan XPS spectra of Nd_2O_3-coated Si-ns films of sample R5.

In all survey spectra, carbon $1s$ (C $1s$) peak, observed at 284.8 eV, was used as a correction reference. This single C $1s$ peak may originate from surface contamination during sample preparation or from the deposition of adventitious hydrocarbon from the instrument itself. From high-resolution XPS spectrum of Fig. 16, we can clearly distinguish Nd $3d$ core level signal of the Nd_2O_3 with its BE doublet Nd $3d_{5/2}$ and Nd $3d_{3/2}$ peaks observed at 980.7 and 1003.2 eV, respectively. The peaks separation value was found to be 22.5 eV, which corresponds to the trivalent neodymium (Nd^{3+}) in Nd-O bonding. [50–52]. In addition, the peak at 122 eV is ascribed to Nd $4d$ of the Nd^{3+} of the same Nd_2O_3 structure. On the other hand, Figure 17 shows

the core level experimental and Gaussian-fitted oxygen O *1s* spectra. Spectrum deconvolution consists of two symmetric peaks. The low-energy state peak (located at 529.7 eV) is assigned to O in Nd_2O_3 molecule [53] and the high-energy state (at 532.9 eV) may be attributed to O in SiO_2 [54].

Table 2.
Binding energies and chemical states of the elements composing un-coated and Nd_2O_3-coated Si-nc.

Peaks	Binding energy (eV)		
	SiN/Si 1100 °C-2 h R2	Nd_2O_3/SiN/Si 900 °C-15 min. R2.5	Nd_2O_3/SiN/Si 900 °C-15 min. R5
O *2s*	21.8	22	26
Si *2p*	98.8	/	/
Nd *4d*	/	122	122
Si*2s*-SiO_2	150.8	/	/
Nd *4p*	/	229	230
C *1s*	284.8	285	285
N *1s*	396.8	/	/
O *1s*	528.8	532	530
Nd (*KLL*)	/	757	759
O (*KLL*)	977.7–998.8	/	/
Nd *3d$_{5/2}$*	/	982	982
Nd*d$_{3/2}$*	/	1005	1004

3.7. PL analysis

The room temperature PL analyses of Nd_2O_3-coated SiN thin films containing Si-ns are presented as a function of various NH_3/SiH_4 gas ratios *R* and annealing temperatures. Two sets of samples were investigated. The first set, comprising samples R2.5, R3, R4, and R5, was annealed at 900 °C for 15 min. The second set (R2 and R4) was thermally annealed at 1100 °C for 2 h. Figure 18 shows room-temperature visible luminescence from silicon nanocrystals for samples prepared at two different NH_3/SiH_4 ratios: *R* = 2 and 4. Spectra reveal identical broad PL signals with a tale spanning almost the whole visible range [55]. The positions of emission peaks and the signal intensity were found to be sensitive to the gas ratio with the more intense signal generated from samples with smaller Si-ns nanostructures sizes (*R* = 4) with a slight blue-light centred downshift occurring in larger Si-ns [56].

Concerning NIR PL and upon 325 nm laser irradiation of samples R2 and R4, we noticed [Fig. 19(a)] strong PL emission peaks centred at 1083 nm related to the intra-*4f* transition $^4F_{3/2} \rightarrow \,^4I_{11/2}$ of Nd^{3+} ions. The second emission peak at 987 nm emerges solely in the spectrum of R2 and could be linked to an existing a-Si phase not found in sample R4. Concerning samples R3 and R5, annealed at a lower temperature and shorter time (900 °C/15 min.) and excited respectively with 374 and 656 nm Xenon radiations, we found that NIR bands of Nd^{3+} ions have shifted to a lower wavelength range [Fig. 19(b)] with peak maxima situated at 1025 and 1031 nm, respectively. The
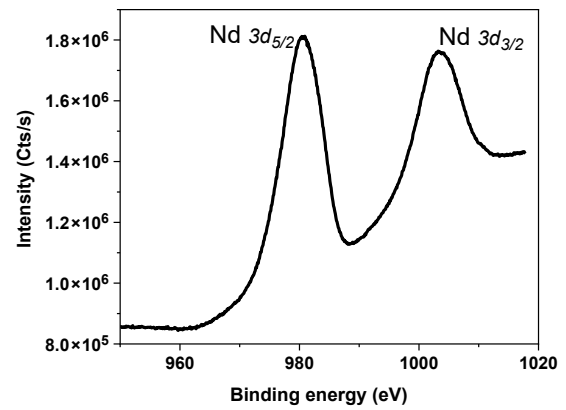

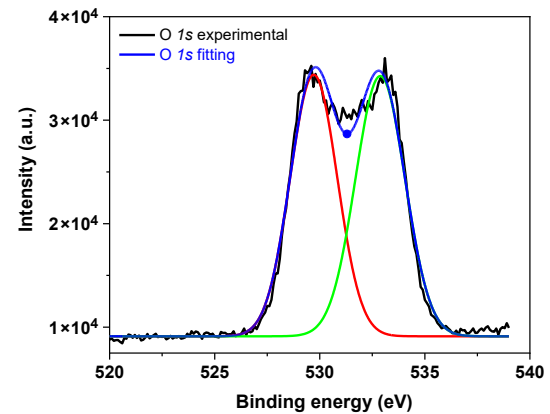**Fig. 16.** High-resolution spectrum of Nd *3d* of sample R2.5.

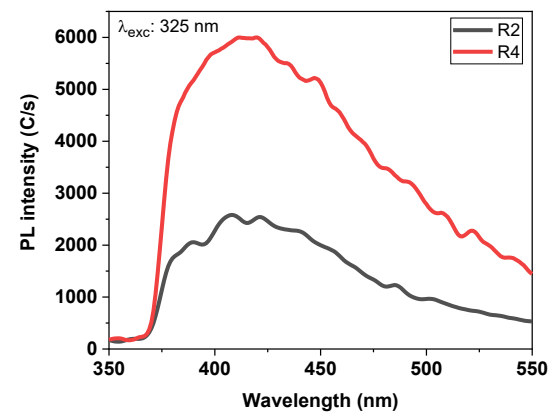**Fig. 17.** High-resolution XPS core level spectra of O *1s*.

Fig. 18. Si-ns visible range PL spectra for samples *R* = 2 and 4.

wavelength increase of the PL peak has been demonstrated by authors where a shift of the Nd emission (from 1025–1031 to 1083 nm) occurs after increasing the annealing temperature [57]. For sample R5, a less intense Nd^{3+} PL line arises at 1358 nm corresponding to the $^4F_{3/2} \rightarrow \,^4I_{13/2}$ transition and appearing under an excitation of 656 nm (red light). On the other hand, R3 spectrum exhibits a signal at 827 nm. It is relatively weak and does not appear for R5 sample. We can allocate it to the $^4F_{5/2} \rightarrow \,^4I_{9/2}$ transition [58–60]. For R5, a signal is recorded at 962 nm within the NIR and was assigned to a-Si [61].

It was also noticed that for both sets of samples annealed at different temperatures, it is the lower excitation wavelength (< 400 nm) that generates a more intense PL signal.
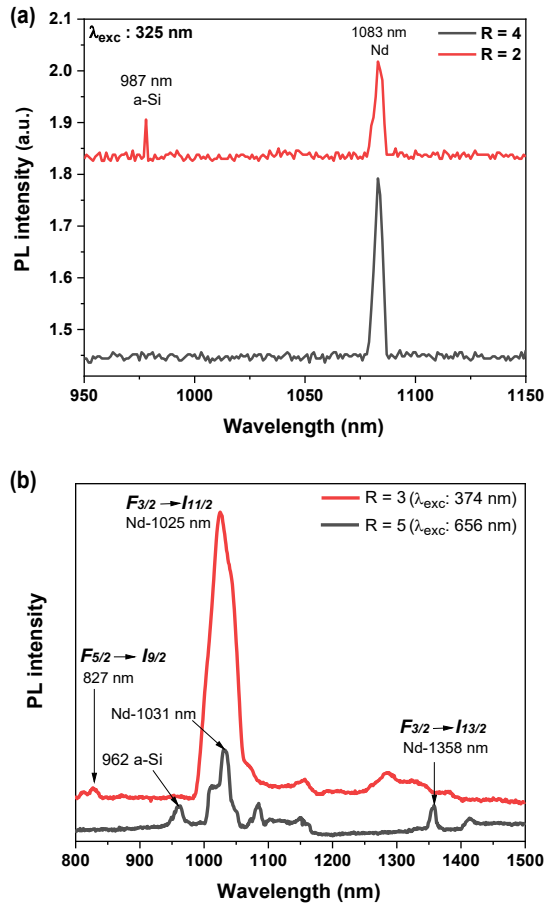
Fig. 19. PL spectra of Nd-coated Si-ns films prepared with different flow ratios: (a) Samples R2 and R4 laser-excited with 325 nm UV light and annealed at 1100 °C for 1 h. (b) R3 and R5 excited with 374 and 656 nm radiations, respectively and annealed at 900 °C for 15 min.

4. Conclusions

In summary, SiN thin films containing Si-ns thin films with different grain sizes using PECVD technique on a Cz-type Si wafer have been successfully prepared. An upper neodymium oxide (Nd_2O_3) coating was deposited on Si-ncs by thermal evaporation. From the results of SIMS and EDS analyses, the authors were able to identify the elemental chemical composition (Si, N, Nd, O) of the thin films. Spectra also revealed good P diffusion in the Si bulk. The nanostructured surface was investigated by AFM and SEM to confirm the formation of Si-nc and the homogenous deposition of Nd_2O_3 layer. Thin films thickness estimations by SEM and profilometry gave values of ~70 and 50–55 nm for SiN and Nd_2O_3, respectively. From XRD data, we determined (*hkl*) crystallographic orientations of the SiN/Nd_2O_3 crystallites and extracted their corresponding average cluster size. Raman spectra demonstrate nanostructures formation depicting the occurrence of a wavenumber downshift of c-Si peaks attributed to grain-size refinement. FTIR spectroscopy revealed the formation of Nd-O, Si-N, Si-O, and Si-H chemical components. Low light-reflectance was observed for Nd_2O_3-coated Si-ns in the VIS-NIR regions which is a desirable optical property for PV applications. In addition, the authors were able to modify optical band gap energies (*Eg*) by the varying NH_3/SiH_4 precursor gas ratio. *Eg* calculations from

diffuse-reflectance spectra showed an increase of *Eg* with decreasing nanostructures size. The authors also reached the conclusion that lower *Eg* values are attributed to SiN (i.e., Si-nc) layers rich in Si. It has been demonstrated that surface functionalization revealed a direct relationship between Si-nc size and *Eg*. XPS analyses made it possible to obtain information on the chemical binding state in Nd_2O_3 and the trivalent state of Nd ions (Nd^{3+}). High-resolution core level of Nd spectra showed a doublet of satellites Nd $3d_{5/2}$ and Nd $3d_{3/2}$ situated at 980.7 and 1003.2 eV, respectively. Finally, PL measurements show that our samples exhibit enhanced luminescent properties. The most intense Nd-related PL peak was obtained for a sample annealed at a temperature of 900 °C. PL emission of the NIR range from Nd^{3+} and its sublayer Si-ns constitute prospective materials for a photovoltaic device.

Authors' statement and contributions

A.M.: SiN PECVD silicon nanostructures realisation, diffusion process, data analysis and paper writing; B.M.: Data analysis and paper writing; N.B.: Data analysis; F.T.: Diffusion process and SiN layers realisation; H.M.: Neodymium evaporation and UV-Vis reflectance measurements; A.N.: Raman spectroscopy measurements; A.M.: SEM and EDS measurements; A.B.: Silicon wafer chemical preparation; S.M.: SIMS measurements; M.D.: XRD measurements.

References

[1] Priolo, F., Gregorkiewicz, T., Galli, M. & Krauss, T. F. Silicon nanostructures for photonics and photovoltaics. *Nat. Nanotechnol.* **9**, 19–32 (2014). https://doi.org/10.1038/nnano.2013.271

[2] Khriachtchev, L., Ossicini, S., Iacona, F. & Gourbilleau, F. Silicon nanoscale materials: From theoretical simulations to photonic applications. *Int. J. Photoenergy* **2021**, 072576 (2012). https://doi.org/10.1155/2012/872576

[3] Zelepukin, I. *et al*. Direct photoacoustic measurement of silicon nanoparticle degradation promoted by a polymer coating. *Chem. Eng. J.* **430**, 132860 (2022). https://doi.org/10.1016/j.cej.2021.132860

[4] Park, Y., Yoo, J., Kang, M. H., Kwon, W. & Joo, J. Photoluminescent and biodegradable porous silicon nanoparticles for biomedical imaging. *J. Mater. Chem. B* **7**, 6271–6292 (2019). https://doi.org/10.1039/C9TB01042D

[5] Schmitt, S. W., Sarau, G. & Christiansen, S. Observation of strongly enhanced photoluminescence from inverted cone-shaped silicon nanostructures. *Sci. Rep.* **5**, 1–12 (2015). https://doi.org/10.1038/srep17089

[6] Hori, T. Structural optimization of silicon thin film for thermoelectric materials. *Sci. Rep.* **11**, 1–9 (2021). https://doi.org/10.1038/s41598-021-01855-6

[7] Leonardi, A. A., Faro, M. J. L. & Irrera, A. Biosensing platforms based on silicon nanostructures: A critical review. *Anal. Chim. Acta* **1160**, 338393 (2021). https://doi.org/10.1016/j.aca.2021.338393

[8] Song, H. Z. & Bao, X. M. Visible photoluminescence from silicon-ion-implanted SiO_2 sfilm and its multiple mechanisms. *Phys. Rev. B* **55**, 6988–6993 (1997). https://doi.org/10.1103/PhysRevB.55.6988

[9] Shimizu-Iwayama, T., Kurumado, N., Hole, D. E. & Townsend, P. D. Optical properties of silicon nanoclusters fabricated by ion implantation. *J. Appl. Phys.* **83**, 6018–6022 (1998). https://doi.org/10.1063/1.367469

[10] Raut, H. K., Ganesh, V. A., Nair, A. S. & Ramakrishna, S. Antireflective coatings: A critical, in-depth review. *Energy & Environ. Sci.* **4**, 3779–3804 (2011). https://doi.org/10.1039/C1EE01297E

[11] Patrone, L. *et al*. Photoluminescence of silicon nanoclusters with reduced size dispersion produced by laser ablation. *J. Appl. Phys.* **87**, 3829–3837 (2000). https://doi.org/10.1063/1.372421

[12] Hessel, C. M. Synthesis of ligand-stabilized silicon nanocrystals with size-dependent photoluminescence spanning visible to near-infrared wavelengths. *Chem. Mater.* **24**, 39–401 (2012). https://doi.org/10.1021/cm2032866

[13] Huang, H. & Zhu, J. J. The electrochemical applications of rare earth-based nanomaterials. *Analyst* **144**, 6789–6811 (2019). https://doi.org/10.1039/C9AN01562K

[14] Sakthivel, P. *et al*. Different rare earth (Sm, La, Nd) doped magnetron sputtered CdO thin films for optoelectronic applications. *J. Mater Sci: Mater. Electron.* **30**, 9999–10012 (2019). https://doi.org/10.1007/s10854-019-01342-9

[15] MacDonald, A. N., Hryciw, A., Lenz, F. & Meldrum, A. Interaction between amorphous silicon nanoclusters and neodymium ions. *Appl. Phys. Lett.* **89**, 173132 (2006). https://doi.org/10.1063/1.2360897

[16] Ye, C., Zhou, L., Wang, X. & Liang, Z. Photon upconversion: from two-photon absorption (TPA) to triplet–triplet annihilation (TTA). *Phys. Chem. Chem. Phys.* **18**, 10818–10835 (2016). https://doi.org/10.1039/C5CP07296D

[17] Sun, Q. C., Ding, Y. C., Sagar, D. M. & Nagpal, P. Photon upconversion towards applications in energy conversion and bioimaging. *Prog. Surf. Sci.* **92**, 281–316 (2017). https://doi.org/10.1016/j.progsurf.2017.09.003

[18] Kenyon, A. J., Trwoga, P. F., Federighi, M. & Pitt, C. W. Optical properties of PECVD erbium-doped silicon-rich silica: evidence for energy transfer between silicon microclusters and erbium ions. *J. Phys. Condensed Matter.* **6**, L319 (1994). https://doi.org/10.1088/0953-8984/6/21/007

[19] Debieu, O. *et al*. Effect of annealing and Nd concentration on the photoluminescence of Nd^{3+} ions coupled with silicon nanoparticles. *J. Appl. Phys.* **108**, 113114 (2010). https://doi.org/10.1063/1.3510521

[20] Bréard, D. *et al*. Spectroscopic studies of Nd^{3+}-doped silicon-rich silicon oxide films. *Mater. Sci. Eng. B* **146**, 179–182 (2008). https://doi.org/10.1016/j.mseb.2007.07.107

[21] Seo, S. Y. & Shin, J. H. The Nd-nanocluster coupling strength and its effect in excitation/de-excitation of Nd3+ luminescence in Nd-doped silicon-rich silicon oxide. *MRS Online Proceedings Library (OPL)* **770**, 610 (2003). https://doi.org/10.1557/PROC-770-I6.10

[22] Benyahia, B. *et al*. Evolution of optical and structural properties of silicon nanocrystals embedded in silicon nitride films with annealing temperature. *J. Nano Res.* **49**, 163–173 (2017). https://doi.org/10.4028/www.scientific.net/JNanoR.49.163

[23] Tiour, F. *et al*. Opto-structural properties of Si-rich SiNx with different stoichiometry. *Appl. Phys. A* **126**, 1–10 (2020). https://doi.org/10.1007/s00339-019-3258-5

[24] Brik, A. *et al*. Annealing Effects on Structural Characteristics of Europium Doped Silicon-Rich Silicon Nitride. *Silicon* **14**, 8417–8425 (2022). https://doi.org/10.1007/s12633-021-01636-w

[25] Lipiński, M., Panek, P., Bielańska, E., Węgłowska, J. & Czternastek, H. Influence of porous silicon on parameters of silicon solar cells. *Opto-Electron. Rev.* **8**, 418–420 (2000).

[26] Makuła, P., Pacia, M. & Macyk, W. How to correctly determine the band gap energy of modified semiconductor photocatalysts based on UV–Vis spectra. *J. Phys. Chem. Lett.* **9**, 6814–6817 (2018). https://doi.org/10.1021/acs.jpclett.8b02892

[27] Molinari, M., Rinnert, H., Vergnat, M. & Weisbecker, P.Evolution with annealing treatments of the size of silicon nanocrystallites embedded in a SiNx matrix and correlation with optical properties. *Mater. Sci. Eng. B Solid State Mater. Adv. Technol.* **101**, 186–189 (2003). https://doi.org/10.1016/S0921-5107(02)00715-8

[28] Takeoka, S., Fujii, M. & Hayashi, S. Size-dependent photoluminescence from surface-oxidized Si nanocrystals in a weak confinement regime. *Phys. Rev. B* **62**, 16820–16825 (2000). https://doi.org/10.1103/PhysRevB.62.16820

[29] Shao, M. *et al*. Effect of deposition temperature on structure and properties of Nd_2O_3 thin films prepared by magnetron sputtering. *Vacuum* **169**, 108936 (2019). https://doi.org/10.1016/j.vacuum.2019.108936

[30] Deshmukh, N. V. *et al*. Photoluminescence and IV characteristics of a CdS-nanoparticles-porous-silicon heterojunction. *Nanotechnology* **12**, 290–294 (2001). https://doi.org/10.1088/0957-4484/12/3/316

[31] Joshi, M., Hu, S. J. & Goorsky, M. S. Porous silicon films for thin film layer transfer applications and wafer bonding. *ECS Trans.* **33**, 195–206 (2010). https://doi.org/10.1149/1.3483508

[32] Bentzen, A., Holt, A., Christensen, J. S. & Svensson, B. G. High concentration in-diffusion of phosphorus in Si from a spray-on source. *J. Appl. Phys.* **99**, 064502 (2006). https://doi.org/10.1063/1.2179197

[33] Hu, S. M., Fahey, P. & Dutton, R. W. On models of phosphorus diffusion in silicon. *J. Appl. Phys.* **54**, 6912–6922 (1983). https://doi.org/10.1063/1.331998

[34] Kaelble, E. F. *Handbook of X-Rays*. (McGraw-Hill, 1967).

[35] Chavan, S. V., Sastry, P. U.M. & Tyagi, A. K. Combustion synthesis of nano-crystalline Nd-doped ceria and Nd_2O_3 and their fractal behavior as studied by small angle X-ray scattering. *J. Alloys Compd.* **456**, 51–56 (2008). https://doi.org/10.1016/j.jallcom.2007.02.019

[36] Yuvakkumar, R. & Hong, S. I. Nd_2O_3: novel synthesis and characterization. *J. Solgel Sci. Technol.* **73**, 511–517 (2015). https://doi.org/10.1007/s10971-015-3629-0

[37] Barbé, J., Makasheva, K., Perraud, S., Carrada, M. & Despax, B. Structural analysis of the interface of silicon nanocrystals embedded in a Si_3N_4 matrix. *J. Phys. D* **47**, 255302 (2014). https://doi.org/10.1088/0022-3727/47/25/255302

[38] Tsu, R. *Defects in Semiconductors*. (North-Holland, 1981).

[39] Smit, C. *et al*. Determining the material structure of microcrystalline silicon from Raman spectra. *J. Appl. Phys.* **94**, 3582–3588 (2003). https://doi.org/10.1063/1.1596364

[40] Gouteron, J., Michel, D., Lejus, A. M. & Zarembowitch, J. Raman spectra of lanthanide sesquioxide single crystals: Correlation between A and B-type structures. *J. Solid State Chem.* **38**, 288–296 (1981). https://doi.org/10.1016/0022-4596(81)90058-X

[41] Jiang, S. *et al*. Anomalous compression behaviour in Nd_2O_3 studied by x-ray diffraction and Raman spectroscopy. *AIP Adv.* **8**, 025019 (2018). https://doi.org/10.1063/1.5018020

[42] Zhang, S. L. *et al*. Raman spectra in a broad frequency region of p−type porous silicon. *J. Appl. Phys.* **76**, 3016–3019 (1994). https://doi.org/10.1063/1.357504

[43] Dreer, S. & Wilhartitz, P. Critical evaluation of the state of the art of the analysis of light elements in thin films demonstrated using the examples of SiO_XN_Y and AlO_XN_Y films. *Pure Appl. Chem.* **76**, 1161–1213 (2004). https://doi.org/10.1351/pac200476061161

[44] Tsu, D. V., Lucovsky, G. & Mantini, M. J. Local atomic structure in thin films of silicon nitride and silicon diimide produced by remote plasma-enhanced chemical-vapor deposition. *Phys. Rev. B* **33**, 7069–7076 (1986). https://doi.org/10.1103/PhysRevB.33.7069

[45] Pai, P. G., Chao, S. S., Takagi, Y. & Lucovsky, G. Infrared spectroscopic study of SiOx films produced by plasma enhanced chemical vapor deposition. *J. Vac. Sci. Technol. A* **4**, 689–694 (1986). https://doi.org/10.1116/1.573833

[46] Bisi, O., Ossicini, S. & Pavesi, L. Porous silicon: a quantum sponge structure for silicon based optoelectronics. *Surf. Sci. Rep.* **38**, 1–126 (2000). https://doi.org/10.1016/S0167-5729(99)00012-6

[47] Sopori, B. L. *et al*. Hydrogen in silicon: A discussion of diffusion and passivation mechanisms. *Sol. Energy Mater. Sol. Cell.* **41**, 159–169 (1996). https://doi.org/10.1016/0927-0248(95)00098-4

[48] Zhang, X. H. *et al*. Non-isothermal kinetic analysis of thermal dehydration of La2(CO₃)₃·3.4HO in air. *T. Nonferr. Soc.* **24**, 3378−3385 (2014). https://doi.org/10.1016/S1003-6326(14)63480-4

[49] Yuvakkumar, R. & Hong, S. I. $Nd_2O_3SC_2$: novel synthesis and characterization. *J. Solgel Sci. Technol.* **73**, 511–517 (2015). https://doi.org/10.1007/s10971-015-3629-0

[50] Jeon, S. H. *et al*. Hydrothermal synthesis of Nd_2O_3 nanorods. *Ceram. Int.* **43**, 1193–1199 (2017). https://doi.org/10.1016/j.ceramint.2016.10.062

[51] Pan, T. M. & Lu, C. H. Forming-free resistive switching behavior in Nd_2O_3, Dy_2O_3, and Er_2O_3 films fabricated in full room temperature. *Appl. Phys. Lett.* **99**, 113509 (2011). https://doi.org/10.1063/1.3638490

[52] Pop, V. *et al*. The influence of milling and annealing on the structural and magnetic behavior of Nd_2Fe14B/α-Fe magnetic nanocomposite. *J. Alloys Compd.* **581**, 821–827 (2013). https://doi.org/10.1016/j.jallcom.2013.07.194

[53] Moulder, J. F., Stickle, W. F., Sobol, P. E. & Bomben, K. D. *Handbook of X-ray Photoelectron Spectroscopy*. (Perkin-Elmer Corporation, 1992)

[54] Pan, Z. J., Zhang, L. T. & Wu, J. S. Electronic structure and transport properties of doped CoSi single crystal. *J. Appl. Phys.* **101**, 033715 (2007). https://doi.org/10.1063/1.2464186

[55] Wilcoxon, J. P. & Samara. G. A., Tailorable, visible light emission from silicon nanocrystals. *Appl. Phys. Lett.* **74**, 3164–3166 (1999). https://doi.org/10.1063/1.124096

[56] Li, X., He, Y. Talukdar, S. S. & Swihart, M. T. Process for preparing macroscopic quantities of brightly photoluminescent silicon nanoparticles with emission spanning the visible spectrum. *Langmuir* **20**, 8490–8496 (2003). https://doi.org/10.1021/la034487b

[57] Iacona, F., Franzò, G. & Spinella, C. Correlation between luminescence and structural properties of Si nanocrystals. *J. Appl. Phys.* **87**, 1295–1303 (2000). https://doi.org/10.1063/1.372013

[58] Chen, G. *et al*. Core/shell $NaGdF_4$: Nd^{3+}/$NaGdF_4$ nanocrystals with efficient near-infrared to near-infrared downconversion photoluminescence for bioimaging applications. *ACS Nano* **6,** 2969–2977 (2012). https://doi.org/10.1021/nn2042362

[59] Yu, X. F. *et al*. Highly efficient fluorescence of NdF_3/SiO_2 core/shell nanoparticles and the applications for in vivo NIR detection. *Adv. Mater.* **20**, 4118–4123 (2008). https://doi.org/10.1002/adma.200801224

[60] Guzik, M., Tomaszewicz, E., Guyot, Y., Legendziewicz, J. & Boulon, G. Structural and spectroscopic characterizations of two promising Nd-doped monoclinic or tetragonal laser tungstates. *J. Mater. Chem.* **22**, 14896–14906 (2012). https://doi.org/10.1039/C2JM30799E

[61] Henderson, E. J. *et al*. Colloidally stable silicon nanocrystals with near‑infrared photoluminescence for biological fluorescence imaging. *Small* **7**, 2507–2516 (2011). https://doi.org/10.1002/smll.201100845